Article

Plasma Actuation for the Turbulent Mixing of Fuel Droplets and Oxidant Air in an Aerospace Combustor

Zhengqi Tai [1,2], Qian Chen [1,2,*], Xiaofei Niu [1,2], Zhenhua Lin [1,2] and Hesen Yang [3]

1 School of Aeronautics and Astronautics, Shenzhen Campus of Sun Yat-sen University, Shenzhen 518107, China
2 School of Aeronautics and Astronautics, Sun Yat-sen University, Guangzhou 510275, China
3 Science and Technology on Plasma Dynamics Laboratory, Air Force Engineering University, Xi'an 710038, China
* Correspondence: chenq289@mail.sysu.edu.cn

Abstract: In order to explore plasma-assisted turbulent mixing in aerospace engines, the dielectric barrier discharge plasma actuation for the turbulent mixing of fuel droplets and oxidant air in a ramjet combustor was studied using computational fluid dynamics. A two-way coupling of turbulent air and discrete droplets was realized by Eulerian–Lagrangian simulation, and the dielectric barrier discharge plasma action on flow was modeled by body force. The results show that the plasma actuation can rearrange the recirculation zone behind the evaporative V-groove flameholder, and the main mechanism of actuation is to increase the local momentum of the fluid; the actuation dimension, actuation intensity, and actuation position of the dielectric barrier discharge plasma have strong effects on the turbulent mixing of fuel droplets and oxidant air; and a relatively optimal turbulent mixing can be achieved by adjusting the actuation parameters.

Keywords: plasma actuation; turbulent mixing; fuel droplets; aerospace combustor; dielectric barrier discharge

1. Introduction

Ramjet engines include subsonic combustion ramjet engines and scramjet engines. For the subsonic combustion ramjet engines, although the flow velocity is lower than that of the scramjet engines, the airflow velocity into the combustion chamber can generally reach a Mach number between 0.2 and 0.3. In order to achieve reliable ignition and stable combustion with high efficiency at higher velocity airflow conditions, various flameholders have been proposed and developed, including a V-groove flameholder, dune standing vortex flameholder, flat-plate flameholder, pneumatic flameholder, and evaporative flameholder, among which the evaporative flameholder has better ignition capacity, wider working range, higher combustion efficiency, and the ability to ignite separately [1]. Due to the above advantages, evaporative flameholders have gained wide application in both turbine and ramjet engines [2–6].

Plasma actuation technology generates plasma by ionizing the gas through a high voltage and frequency power to induce additional flow of fluid and accelerate chemical reactions by applying kinetic, thermal, and chemical actions to the neutral gas through the plasma. According to Li et al. [7], this technology is expected to provide breakthrough technology support for advanced aircraft/engine development based on active flow and combustion control. Due to the superior nature of plasma actuation, with a short response time, wide actuation band, and no moving parts, it is being widely studied by scholars, and the main directions of the research are dielectric barrier discharge (DBD), surface arc discharge, etc. Among them, DBD plasma actuation technology has received extensive attention in simulations [8–14], experiments [15–22], and mechanism studies [23–29]. The

main working principle of this technology is flow control by inducing additional velocity of the fluid in the actuation region through the momentum effect of plasma actuation.

Recently, Ombrello et al. [30] studied the effect of plasma discharge on the ignition process, ignition delay time, flame propagation velocity, and combustion chamber flow field. Jin et al. [31] developed a two-dimensional mathematical model of the effect of DBD plasma on the atmospheric combustion of methane–air mixtures, which can well predict the adiabatic flame temperature in the combustion chamber. In addition, it was found that plasma can accelerate the diffusion and mixing of reactants, thus reducing the turbulent mixing time. Cui et al. [32] investigated the optimal delay time for the flammability limit at different plasma frequencies and fuel types. It was found that for methane and propane, the optimal delay time for plasma enhancement precedes the flux pulsation when the flame starts to extinguish. The ignition limit of a methane–air flame can be extended from 0.63 to 0.45 at a specific frequency. Huang et al. [33] showed that plasma actuation can promote kerosene atomization, achieve uniform distribution of kerosene, and improve the ignition limit by forming a rotating arc discharge plasma column between the electrodes and the evaporative flameholder fins in a ramjet combustor. Based on their work, it is necessary to explore other plasma actuation technology potential in this kind of combustor. In the present paper, the cold flow field of a kerosene injection combustor with an evaporative V-groove flameholder is used as the basic flow field, and the modulation effect of DBD plasma actuation on the cold flow field of a kerosene injection combustor with an evaporative V-groove flameholder is investigated by introducing plasma actuation of different dimensions, plasma actuation with different intensities, and plasma actuation at different positions.

The remainder of this paper is organized as follows: We first outline the numerical simulation method in Section 2, including the two-phase-flow mathematical model and the DBD mathematical model. To determine whether the DBD mathematical model can provide accurate flow field characteristics, a numerical simulation on flat-plate flow field is performed in this section and the results are verified with the literature. Section 3 gives results on numerical simulation of ramjet combustor and discussions on turbulent mixing of fuel droplets and oxidant air with different plasma actuation parameters. Finally, the conclusions are summarized in Section 4.

2. Numerical Simulation Method

2.1. Mathematical Model of Two-Phase Flow

The focus of this paper is on the plasma actuation for the turbulent mixing of fuel droplets and oxidant air. The numerical simulation contains gas and liquid droplets. The gaseous phase compressible Reynolds-averaged equations are as follows:

$$\frac{\partial \rho}{\partial t} + \frac{\partial}{\partial x_i}(\rho u_i) = 0 \tag{1}$$

$$\frac{\partial}{\partial t}(\rho u_i) + \frac{\partial}{\partial x_j}(\rho u_i u_j) = -\frac{\partial p}{\partial x_i} + \frac{\partial}{\partial x_j}(-\rho \overline{u_i' u_j'}) + F_i + \frac{\partial}{\partial x_j}[\mu(\frac{\partial u_i}{\partial x_j} + \frac{\partial u_j}{\partial x_i} - \frac{2}{3}\delta_{ij}\frac{\partial u_l}{\partial x_l})] \tag{2}$$

$$\frac{\partial}{\partial t}(\rho E) + \frac{\partial}{\partial x_i}[u_i(\rho E + p)] = \frac{\partial}{\partial x_j}\left[(k + \frac{c_p \mu_t}{\mathrm{Pr}_t})\frac{\partial T}{\partial x_j} + u_i(\tau_{ij})_{eff}\right] + S_h \tag{3}$$

$$\frac{\partial(\rho Y_s)}{\partial t} + \frac{\partial(\rho Y_s u_j)}{\partial x_j} = \frac{\partial}{\partial x_j}\left(\rho D_s \frac{\partial Y_s}{\partial x_j}\right) + \dot{S}_{Y_s} + \dot{\omega}_s \tag{4}$$

where ρ, t, p, μ, E, k, T, and c_p denote density, time, pressure, dynamic viscosity, total internal energy, heat transfer coefficient, temperature, and specific heat capacity, respectively. Here, u_i is the velocity component in three directions (i = 1,2,3); δ_{ij} is the Kronecker function; $(\tau_{ij})_{eff}$ is the strain rate tensor; F_i is the body force source term in the i direction; Y_s and

D_s are the mass fraction and diffusion coefficients, respectively, of the s component; the component number $s = 1, 2, 3, \ldots, N_s - 1$; and N_s is the total number of components.

The Reynolds stress term in the above gaseous phase compressible Reynolds-averaged equations needs to be closed by a turbulence model, and the standard $k–\varepsilon$ turbulence model is used in this paper.

The liquid phase equation is given as follows:

$$\frac{dX_d}{dt} = U_d \tag{5}$$

$$\frac{dU_d}{dt} = \frac{F_d}{m_d} = \frac{f_1}{\tau_d}(U_{seen} - U_d) \tag{6}$$

$$\frac{dT_d}{dt} = \frac{Nu}{3Pr}\frac{C_{p,g}}{C_{p,l}}\frac{f_2}{\tau_d}(T_{seen} - T_d) + \frac{L_V}{C_{p,l}}\frac{\dot{m}_d}{m_d} \tag{7}$$

$$\frac{dm_d}{dt} = \dot{m}_d = -\frac{Sh}{3Sc}\frac{m_d}{\tau_d}\ln(1 + B_M) \tag{8}$$

where X_d, U_d, U_{seen}, T_{seen}, and $C_{p,g}$ denote the position vector of the droplet in the flow field, the velocity vector, and the flow velocity, temperature, and specific heat capacity of the gas around the droplet, respectively. Here, Nu, Pr, Sc, $C_{p,l}$, L_V, f_2, and B_M are the Nusselt number, Sherwood number, Prandtl number, Schmidt number, liquid-phase-specific heat capacity, latent heat of evaporation of liquid droplets, heat transfer correction factor due to evaporation, and Spalding mass transport coefficient, respectively. In this paper, the KH/RT model is used to calculate the breakdown of kerosene droplets.

2.2. DBD Plasma Actuation Model

A schematic diagram of the structure of DBD plasma actuation is shown in Figure 1. Exposed and covered electrodes were installed above and at the bottom of the insulating media barrier layer, respectively. When the voltage and frequency (amplitude of 5–40 kV and frequency of 1–20 kHz [34]) applied at both ends of the electrode were high enough, the air on the upper surface of the covered electrode was weakly ionized with a large number of charged particles, which were driven by the electric field force and collided with the neutral gas, inducing the gas to flow downstream. The mainstream view on the mechanism of DBD plasma actuation induced flow is the "momentum injection effect." According to this mechanism, researchers carried out a corresponding simplification study; the simplification method was mainly conducted by decomposing the momentum exchange rate in unit volume of the DBD induced injection flow field into x direction component and y direction component, and adding to the momentum equations through the form of source terms, to simulate the DBD plasma actuation effect.
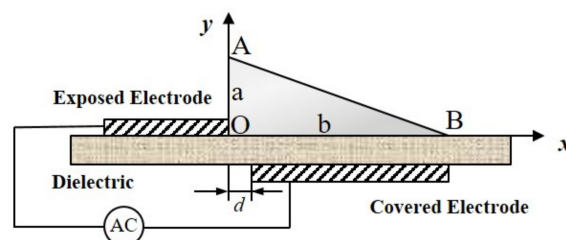
Figure 1. Schematic diagram of DBD plasma actuation structure.

The phenomenological modeling proposed by Shyy et al. [9] is one of the commonly used modeling methods, with the advantages of fast calculation and accurate results, which were used in this study to simulate the effect of plasma on the modulation of the cold flow field in a kerosene-injected combustion chamber with an evaporative V-groove flameholder. As shown in Figure 1, with the Shyy model, the electric field force is located in a triangular

area on the upper surface of the covered electrode and is uniformly linearized. The electric field intensity is greatest near the edge of the exposed electrodes as $E_0 = U_0/d$, U_0 is the voltage applied between the electrodes, and $d = 0.25$ mm is the distance between the two electrodes. As the distance away from the O point increases, the electric field intensity gradually decreases. The equation of the electric field intensity is as follows:

$$\left|\overrightarrow{E}\right| = E_0 - n_1 x - n_2 y \tag{9}$$

where n_1 and n_2 are constants. These are defined as follows:

$$n_1 = (E_0 - E_b)/b \tag{10}$$

$$n_1 = (E_0 - E_b)/a \tag{11}$$

where $E_b = 30$ kV/cm is the breakdown electric field intensity, the height a of the triangular area is 1.5 mm, and the length b is 3 mm. The electric field intensity in the x and y direction components can be expressed as:

$$E_x = \frac{E n_2}{\sqrt{n_1{}^2 + n_2{}^2}} \tag{12}$$

$$E_y = \frac{E n_1}{\sqrt{n_1{}^2 + n_2{}^2}} \tag{13}$$

The body force generated by the DBD plasma actuation in the x and y directions are given as:

$$F_x = E_x \rho_c e_c \alpha \delta \vartheta \Delta t \tag{14}$$

$$F_y = E_y \rho_c e_c \alpha \delta \vartheta \Delta t \tag{15}$$

where ρ_c (= 10^{17} m^{-3}) is the charge density, e_c (= 1.602×10^{-19}) is the meta-charge, α is the charge collision efficiency factor, δ is the Dirac function (located in the triangular region where the body force exists, otherwise it is 0), ϑ is the frequency of the applied voltage, and Δt is the time of the plasma action in one actuation cycle of a radio frequency AC voltage.

2.3. Numerical Simulation Implementation Method

For the numerical simulation of the combustor, the continuity equation, momentum equation, energy equation, and component transport equation of the gaseous phase were solved simultaneously and implicitly. Next, the turbulence model transport equations were solved implicitly; then, the liquid-phase equations were solved, and the source terms of the gas-phase equations were updated; these steps were repeated until convergence of the flow field was reached. The main transport equation and the turbulence model transport equation were spatially discretized using the second-order upwind scheme. The gradient was calculated using the least-squares method based on grid cells. The Roe flux differential split scheme was adopted for the convection flux.

In the numerical simulation of the plasma actuation of the spray field in the combustor carried out in Section 3, in order to enhance the stability of the numerical simulation of the two-phase flow field, the numerical simulation of the pure airflow in the combustor was carried out first. After obtaining the converged flow field, the liquid kerosene fuel was injected, and the numerical simulation studies on the spray field (without and with plasma actuation) in the combustor were carried out.

2.4. Validation of Numerical Simulation Method

In order to obtain satisfactory plasma actuation, the phenomenological model proposed by Shyy et al. [9] was validated numerically. The computation domain and geometry model are consistent with that study, as shown in Figure 2.
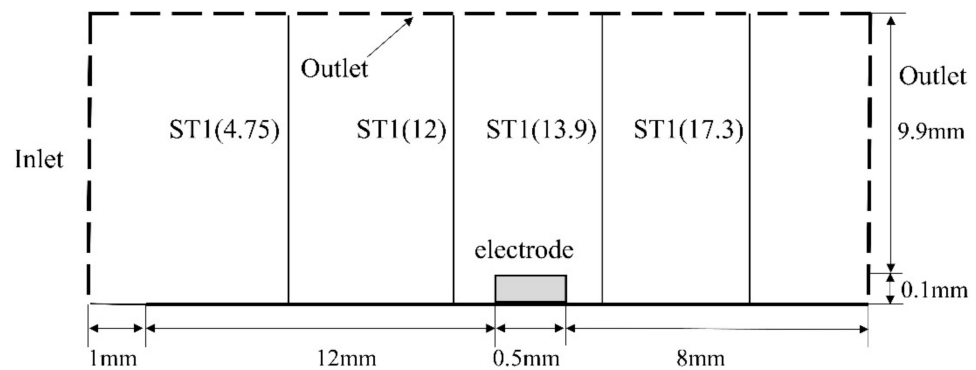
Figure 2. Schematic diagram of calculation domain.

The height of the computational domain was 10 mm, and the distance between the inlet and outlet was 21.5 mm. The flat plate, at a distance of 1 mm from the inlet, constituted the bottom of the computational domain. The exposed electrode, with a length of 0.5 mm and a height of 0.1 mm, was mounted at a distance of 12 mm from the top of the plate. The mesh of the computational domain is shown in Figure 3, and the grid near the electrodes was refined to observe the effect of DBD plasma actuation on the flow field. The number of cells for the plate was 180 thousand. The velocity inlet was used as the inlet boundary condition, and the pressure outlet was used as the outlet boundary condition. The upper wall surface was set as the slip boundary condition, and the lower wall surface had two boundary conditions: the 1 mm length area from the front edge of the plate to the left boundary of the grid was set as the slip boundary condition, and the plate was set as the no-slip boundary condition.
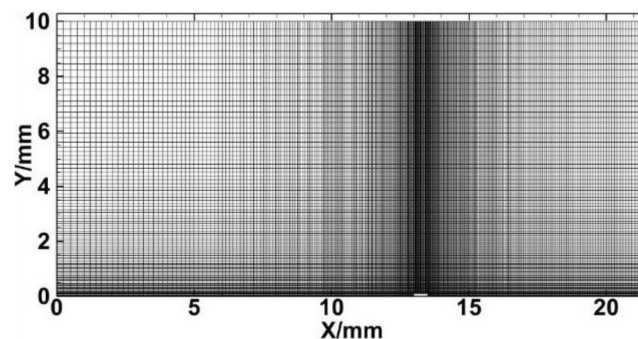
Figure 3. Computational grid.

The velocity distributions at four different locations for inlet parameters of 3 kHz, 4 kV, and 5 m/s are provided in Figure 4, and the results are in agreement with the paper by Shyy et al. [9]. It can be seen that the velocity reaches a maximum downstream from the electrode, and the extent to which the velocity exceeds the free flow velocity indicates the intensity of the plasma actuation; and, in general, the velocity structure downstream from the electrode is similar to that of a wall jet. In addition, it can be seen from Figure 5 that the wall shear stress in the presence of the plasma actuation is larger than that without the plasma actuation. The flow velocity gradually decreases to the free flow velocity away from the wall, which explains the reason that the wall shear stress is negative. The wall shear stress profiles at different frequencies and voltages are given in Figure 5a,b, respectively, and it can be seen that the peak value of the corresponding shear stress becomes larger as the voltage and frequency increase. Wall shear stress profiles for different inlet flow velocities (5 m/s and 2 m/s) at the same actuation voltage and frequency are presented in Figure 5c,d, where the shear stress is dimensionless in terms of the corresponding maximum shear stress without plasma actuation. Here, V_∞ = 2 m/s achieves a larger peak, indicating

that the corresponding effect of the induced generated wall jet increases with decreasing free flow velocity.
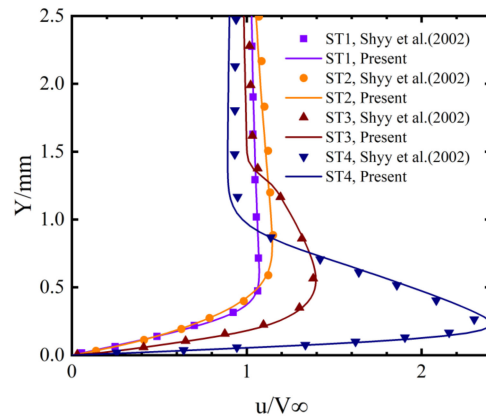
Figure 4. Velocity profiles at four different locations.
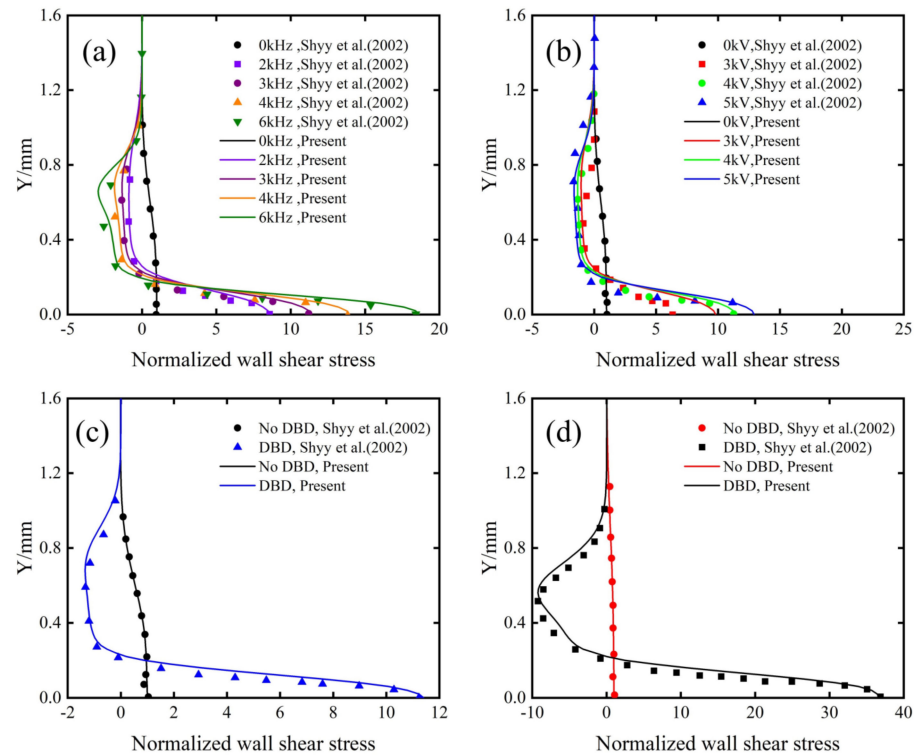
Figure 5. Effects of different parameters on wall shear stress at ST4. (**a**) Frequency, (**b**) voltage, (**c**) inlet velocity with 5 m/s, (**d**) inlet velocity with 2 m/s.

The root mean square error (RMSE) was used to assess the distance between the current simulation results and Shyy et al. [9]. RMSE is given as follows:

$$RMSE = \sqrt{\frac{\sum_{i=1}^{n}\left(X_{present,i} - X_{Shyy,i}\right)^2}{n}} \qquad (16)$$

where X denotes normalized velocity u of Figure 4 and normalized wall shear stress of Figure 5, respectively. Table 1 provides the velocity RMSE of the baseline model at different flow locations; the RMSE at different locations is very small, which implies that the current numerical simulation method is quite reliable. At the same time, the RMSE for shear

stresses with different parameters in Table 2 is also very small relative to the normalized wall shear stress results. Overall, the results are in better agreement with those in the paper of Shyy et al. [9]. For the combustor flow field simulation in Section 3, computation results are not compared with experiment results, because there are no turbulent mixing experiment data available for these aerospace combustors.

Table 1. The RMSE of velocity profiles at four different locations.

Location	ST1	ST2	ST3	ST4
RMSE	0.0101	0.0097	0.0254	0.0567

Table 2. RMSE of normalized wall shear stress with different parameters.

Frequency	RMSE	Voltage	RMSE	V_∞ = 5 m/s	RMSE	V_∞ = 2 m/s	RMSE
0 kHz	0.0491	0 kV	0.0491	No DBD	0.0104	No DBD	0.0654
2 kHz	1.0853						
3 kHz	1.5048	3 kV	1.6115				
4 kHz	1.6202	4 kV	1.3871	DBD	1.2720	DBD	4.4923
6 kHz	2.5094	5 kV	0.6133				

3. Results and Discussion

3.1. Basic Characteristics of the Spray Field in the Combustor

In the subsonic combustion ramjet combustor, although the incoming Mach number ahead of the holder was less than 0.3, the velocity at the trailing edge of the holder was generally greater than Mach number 0.3 because of the relatively large blockage of the holder, so the flow field was treated as a flow of compressible viscous fluid [1].

The flameholder model is illustrated in Figure 6b, and the local and overall grids of the flow field are shown in Figure 6a,c. The length and width of the combustion chamber were 1487 mm and 140 mm, respectively, and the evaporation tube was located in the center of the combustion chamber. The rest of the flow field grid parameters were similar to those used in Xu [1]. Since the fuel mixing and combustion occurred mainly in the evaporation tube location (purple area) and its wake area (red area), these two parts were refined. To accommodate the complex shape of the flameholder, the computational domain was divided using an unstructured grid. The refining of the regions was beneficial for capturing more flow details. The number of cells in the whole combustion chamber was 0.3 million. The maximum dimensions of the purple, red, and green regions were 0.5 mm, 1 mm and 5 mm, respectively, and the boundary layer of the flameholder wall was also refined. To make the simulation results more general, the working conditions of Huang et al. [33] were used. The inlet Mach number was 0.2, the inlet static pressure was 70 kPa, the inlet static temperature was 357 K, the kerosene injection position was 11 mm upstream of the evaporation tube circle, and the kerosene injection used the upper and lower holes simultaneously to ensure that the kerosene was evenly distributed up and down with the airflow movement into the evaporation tube, which is more consistent with the actual situation. The numerical simulation of the plasma on the spray mist field of the evaporation tube was constant. The air flow field velocity contour, velocity vector, and kerosene droplets distribution in the situation of the equivalent ratio of 0.4 for injection are shown in Figure 7, from which it can be seen that the kerosene droplets are uniformly distributed on the upper and lower sides of the V-groove, and the evaporation tube plays the role of slowing down the kerosene droplets and increasing their evaporation time.
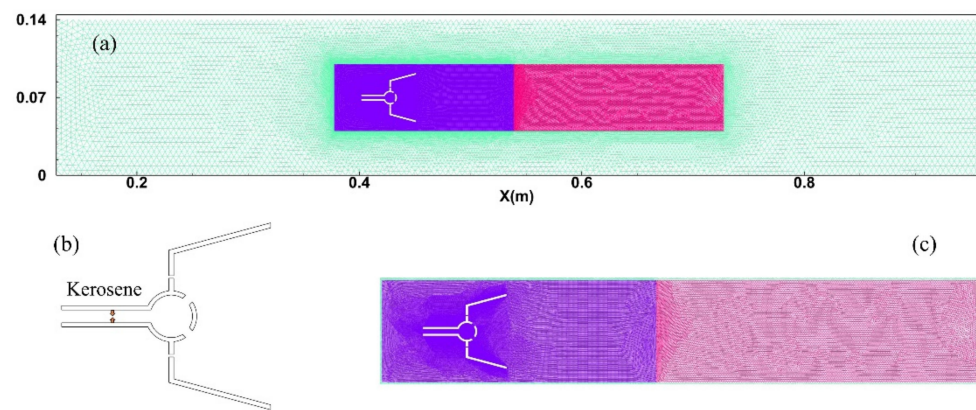
Figure 6. Flameholder structure and grid: (**a**) whole grid of combustor, (**b**) flameholder structure, (**c**) local grid of flameholder.
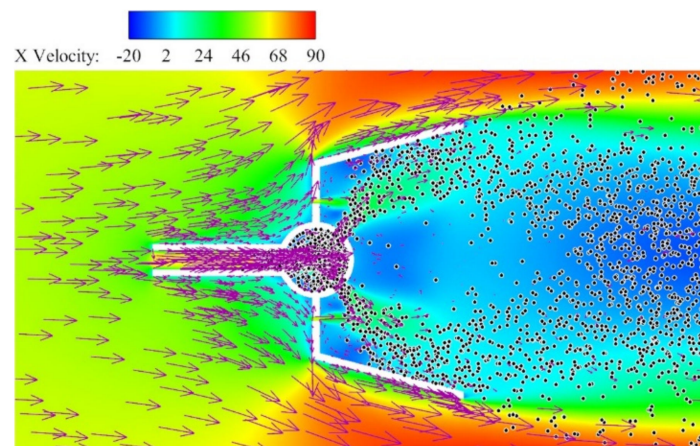
Figure 7. The basic characteristics of the spray field.

3.2. Plasma Actuation of the Spray Field in the Combustor

This section focuses on the effects of different plasma actuation dimensions, intensities, and positions on the air flow field and kerosene droplet distribution.

3.2.1. Actuation Dimensions

The different actuation dimensions are depicted schematically in Figure 8, where DBD plasma actuation with covered electrode lengths of 20 mm, 10 mm, and 5 mm are evenly arranged on the upper and lower wall inner surface of the V-groove.
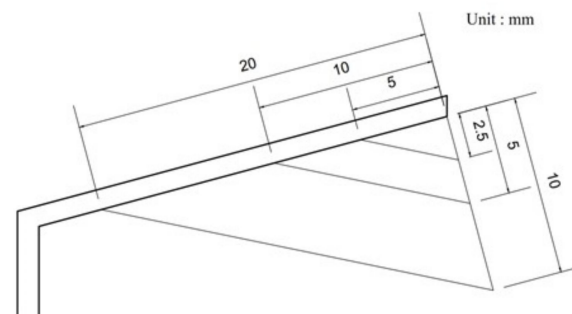
Figure 8. Different actuation dimensions (only the upper wall of the V-groove is shown).

We have analyzed the effects of different actuation dimensions on the spray field in the combustor under three different actuation intensities, and the actuation parameters are shown in Table 3.

Table 3. Different actuation dimensions.

| Actuation Intensity | Actuation Dimensions on Inner Surface | | |
	Length 1 (mm)	Length 2 (mm)	Length 3 (mm)
85 kV, 14 kHz	20	10	5
45 kV, 14 kHz	20	10	5
5 kV, 14 kHz	20	10	5

The effects of different actuation dimensions on the actuation of the spray field are demonstrated in Figures 9–11. In Figure 9, it can be seen that the region and velocity of the induced jet increase with the increase in the actuation dimensions at the same actuation intensity. In the case of the inner surface actuation length of 20 mm, the plasma actuation forms a recirculation zone inside the flameholder. Due to the excessive velocity, the kerosene droplets all gather to the midline position of the flameholder, with the result that most of the droplets cannot flow out from the outlet of the evaporation tube and can only flow out from the inlet of the evaporation tube in the reverse direction, which has a harmful impact on stabilizing the flame and improving the combustion efficiency. When the inner surface actuation length is 10 mm, the region affected by the DBD plasma actuation and the induced velocity is significantly reduced. At the same time, kerosene droplets flowing out of the evaporation tube nozzles are entrained by the recirculation zone to the middle position before intersecting at the position downstream of the evaporation tube, and finally, the droplets are propelled out of the flameholder by the recirculation zone. With the inner surface actuation length of 5 mm, the DBD plasma actuation-induced jet can only affect the shape of the recirculation zone after the evaporation tube in a small region. The kerosene droplets do not touch the V-groove fins because of the recirculation zone near the wall, and they flow directly out of the flameholder. Finally, similar results to those in Figure 9 can be observed in Figures 10 and 11. With other plasma actuation conditions being the same, the larger the actuation dimensions, the larger the induced velocity and recirculation zone generated, and ultimately the effect on the flow field is more significant. It is interesting that in Figure 11b a fine mixing is obtained.

(**a**)

Figure 9. *Cont.*

(**b**)

(**c**)
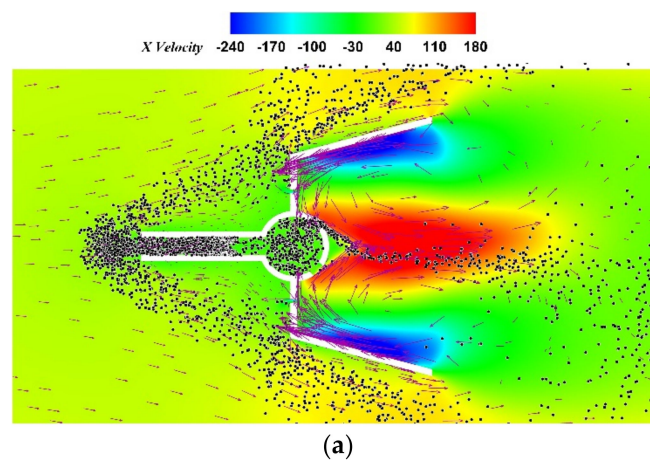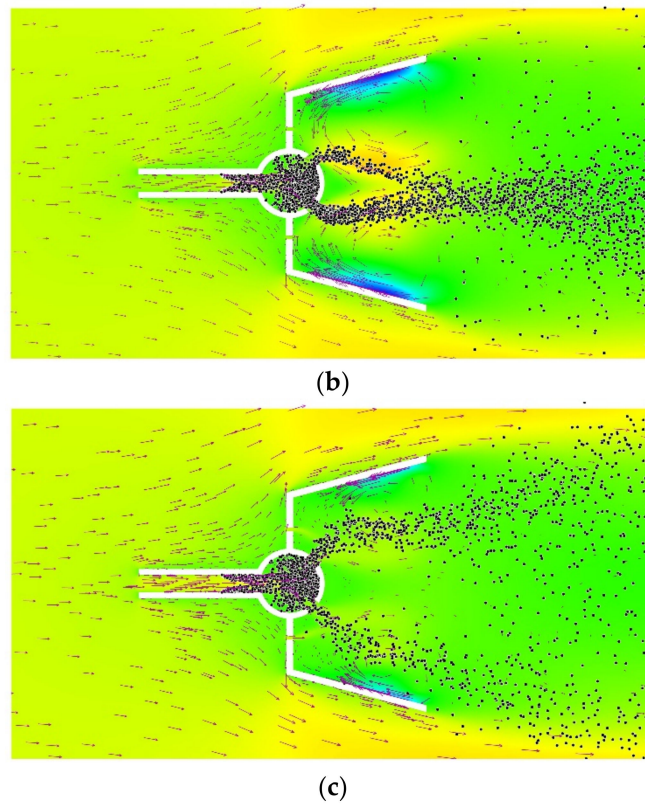
Figure 9. Spray field at different actuation dimensions: (**a**) 20 mm, (**b**) 10 mm, (**c**) 5 mm with 85 kV and 14 kHz.

(**a**)

(**b**)
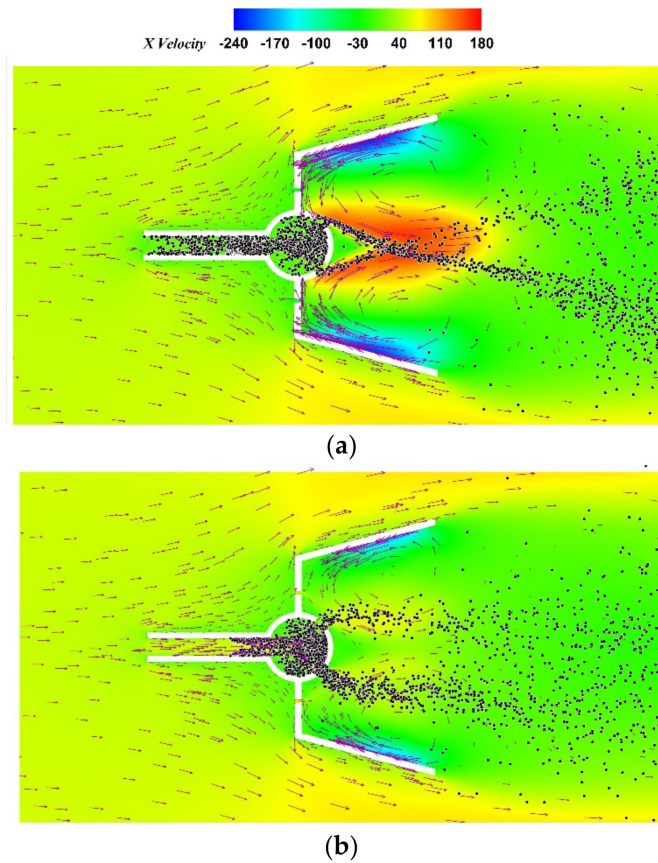
Figure 10. *Cont.*
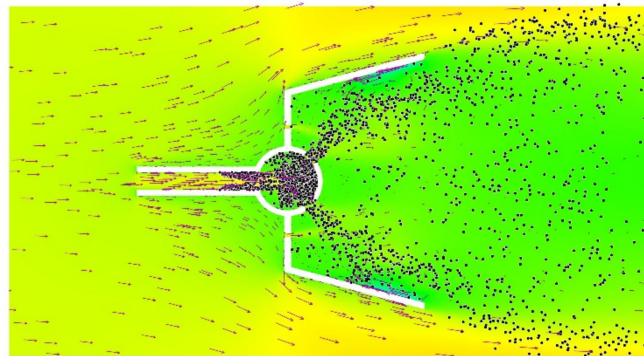
(**c**)

Figure 10. Spray field at different actuation dimensions: (**a**) 20 mm, (**b**) 10 mm, (**c**) 5 mm with 45 kV and 14 kHz.
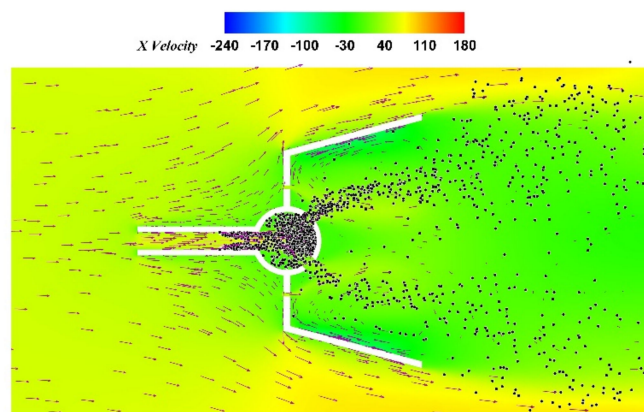
(**a**)
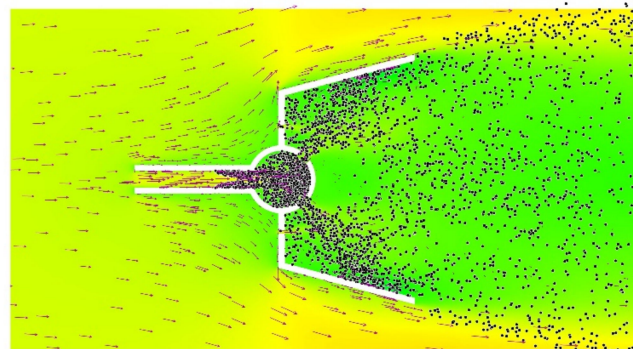
(**b**)
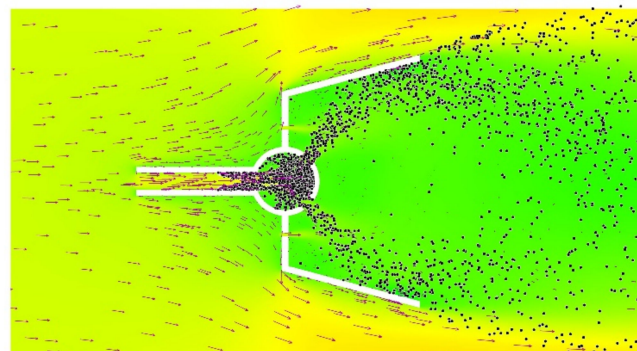
(**c**)

Figure 11. Spray field at different actuation dimensions: (**a**) 20 mm, (**b**) 10 mm, (**c**) 5 mm with 5 kV and 14 kHz.

3.2.2. Actuation Intensities

In this section, the effects of different actuation intensities on the gas-phase flow field and kerosene droplet distribution for actuation lengths of 20, 10, and 5 mm at the inner surface of the flameholder (the actuation position is shown in Figure 10) are investigated. The actuation parameters for the different intensities are summarized in Tables 4 and 5.

Table 4. Different actuation intensities with 20 mm actuation length on inner surface.

Work Conditions	Voltage (kV)	Frequency (kHz)
a	85	14
b	85	9
c	85	5
d	45	14
e	45	9
f	45	5
g	5	14
h	5	9
i	5	5

Table 5. Different actuation intensities with 10 mm and 5 mm actuation lengths on inner surface.

Work Conditions	Voltage (kV)	Frequency (kHz)
a	5	14
b	45	14
c	85	14

The spray field of different actuation intensities is shown in Figure 12, whereas the case in Figure 12a has been discussed in Section 3.2.1 and will not be repeated here. As shown in Figure 12a,b, with large actuation intensity, the induced velocity generated by the plasma actuation far exceeds the velocity at the outlet of the evaporation tube, forcing the kerosene droplets to flow out from the evaporation tube inlet instead of the exit, which is not conducive to the evaporation and combustion of kerosene droplets. For operating conditions (c) and (d), it can be seen that the velocity generated by DBD plasma actuation is still slightly on the high side, and the kerosene droplets are gathered in the center of the V-groove by the induced airflow, which accelerates the velocity of the kerosene droplets and reduces the contact time between the kerosene and air. At the same time, the concentration of a large number of droplets in the center leads to a local fuel enrichment, which is unfavorable to ignition. Observing the remaining five working conditions (Figure 12e–i), it can be found that as the actuation intensity gradually decreases, the DBD-induced velocity also gradually decreases, and the airflow returns from the end of the V-groove fin plate to the exit position of the evaporation tube, which is conducive to increasing the heat exchange between high-temperature air and kerosene, increasing the air–fuel ratio and reducing the ignition delay time.
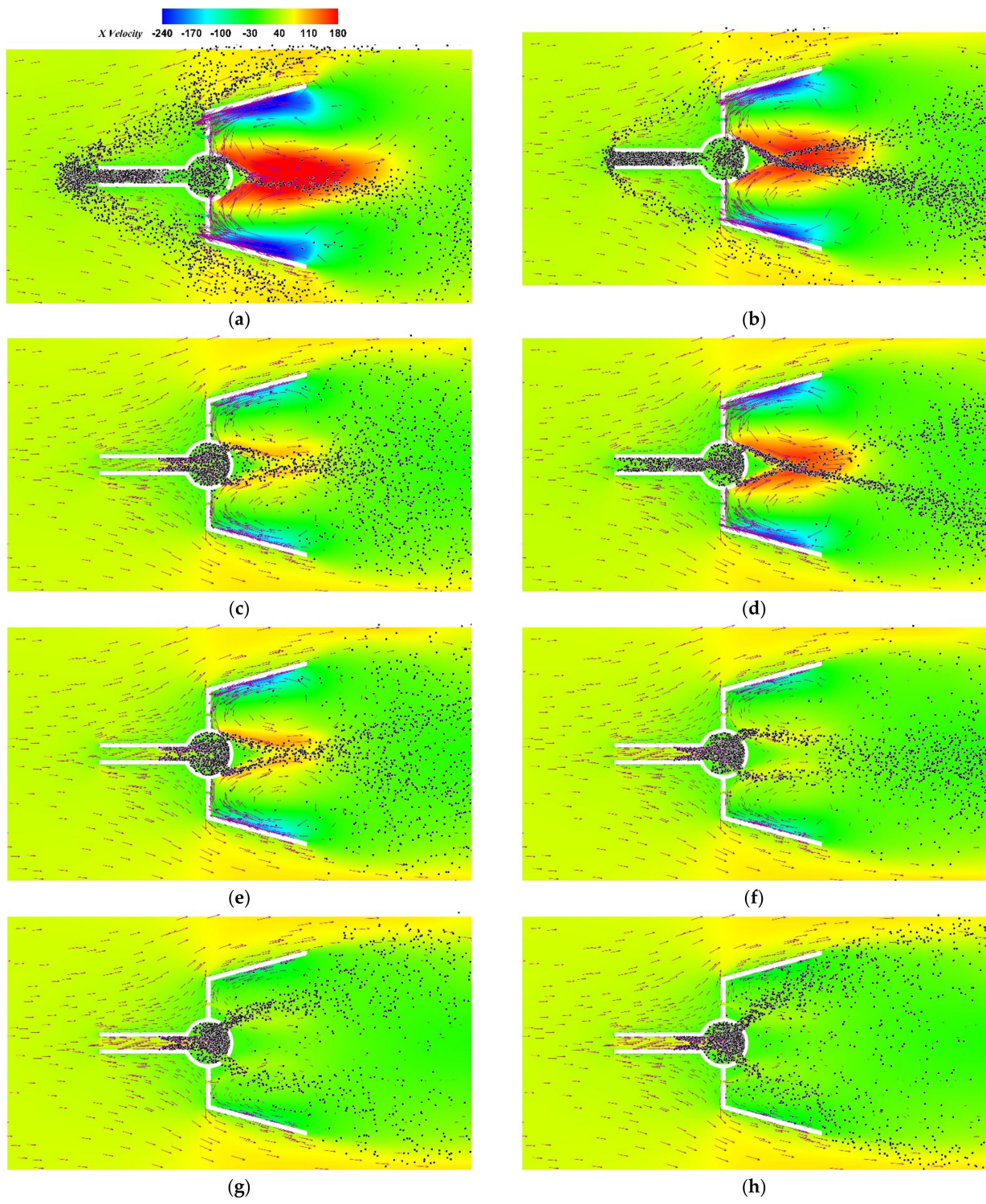
Figure 12. *Cont.*
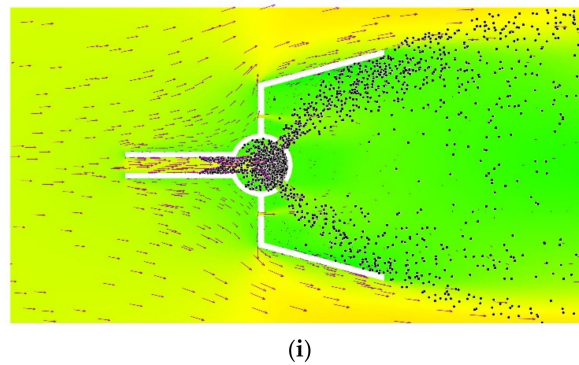
(i)

Figure 12. Spray field under different actuation intensities with 20 mm actuation length on inner surface: (**a**) 85kV, 14kHz, (**b**) 85kV, 9kHz, (**c**) 85kV, 5kHz, (**d**) 45kV, 14kHz, (**e**) 45kV, 9kHz, (**f**) 45kV, 5kHz, (**g**) 5kV, 14kHz, (**h**) 5kV, 9kHz, (**i**) 5kV, 5kHz.

Figures 13 and 14 provide the spray fields for inner surface actuation lengths of 10 mm and 5 mm, respectively (actuation positions are shown in Figure 8), and the actuation parameters for the different intensities are given in Table 5. As illustrated in Figure 13, the DBD plasma actuation induces an increase in the wall jet velocity as the plasma actuation intensity increases. Figure 13a demonstrates that the distribution region of kerosene droplets is greater compared to other operating conditions, and some of the kerosene droplets flow back inside the flameholder, which can increase the contact time between the kerosene droplets and the air, thus further facilitating kerosene ignition and combustion. For the contour of the spray field in the flameholder in Figure 13b,c, it can be seen that the kerosene droplets cannot be uniformly distributed in the rear region of the V-groove due to the increase in the induced velocity caused by the excessive actuation intensity and the formation of kerosene droplet aggregation. The heating effect of high temperature backflow on kerosene droplets is reduced, which is not helpful for the evaporation of kerosene. At the same time, the backflow generated by the actuation induction accelerates the speed of the kerosene droplet outflow, and the contact time with the air becomes shorter, which is not beneficial for ignition and combustion.

(a)

Figure 13. *Cont.*

(**b**)

(**c**)
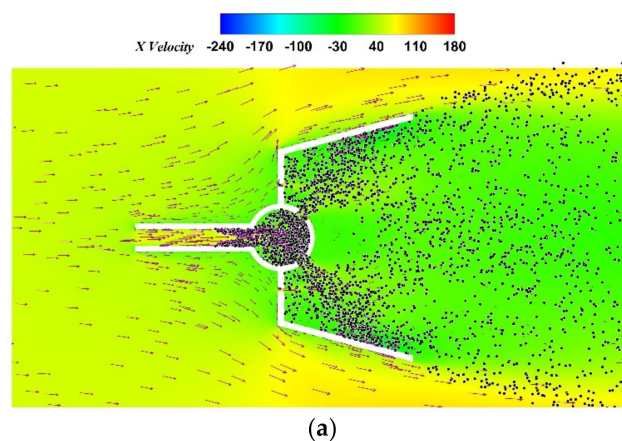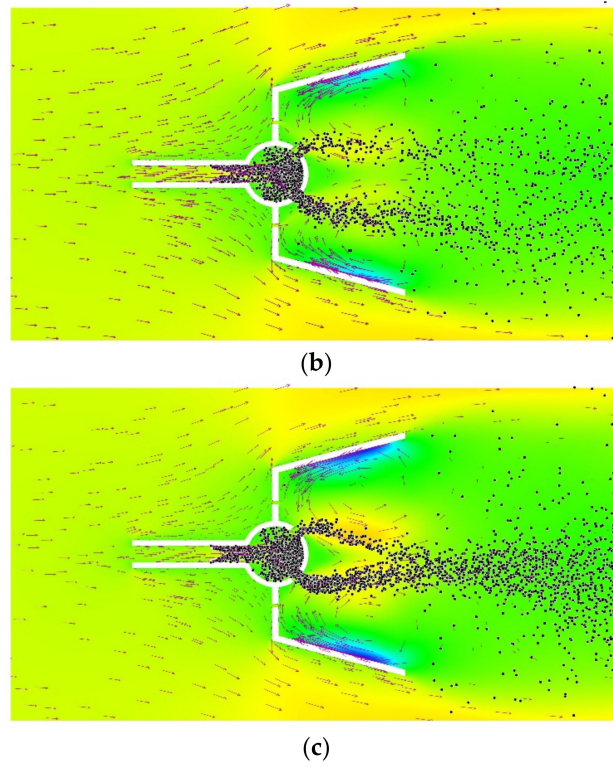
Figure 13. Spray field under different actuation intensities with 10 mm actuation length on inner surface: (**a**) 5kV, 14kHz, (**b**) 45kV, 14kHz, (**c**) 85kV, 14kHz.

(**a**)

(**b**)

Figure 14. *Cont.*

(**c**)
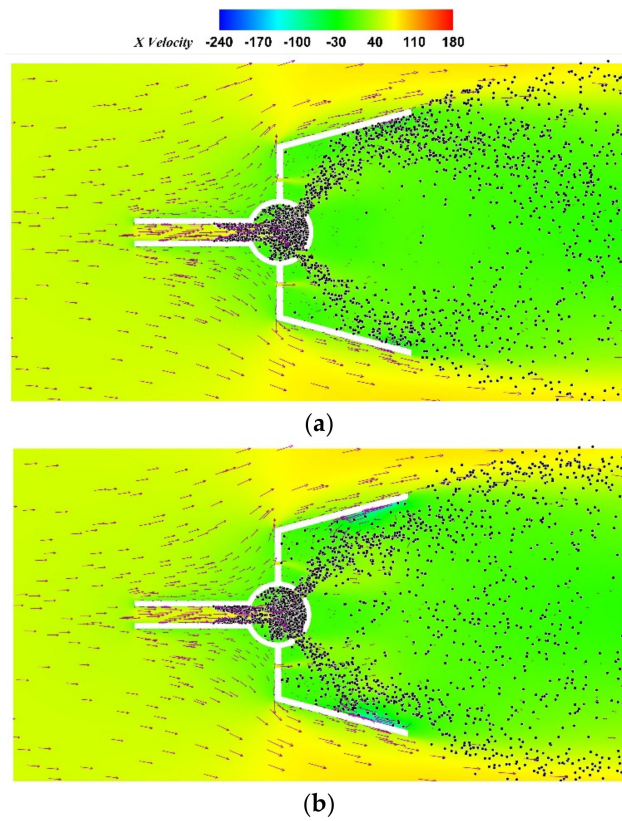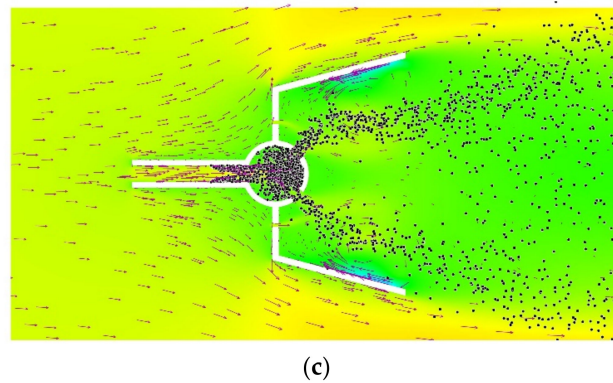
Figure 14. Spray field under different actuation intensities with 5 mm actuation length on inner surface: (**a**) 5kV, 14kHz, (**b**) 45kV, 14kHz, (**c**) 85kV, 14kHz.

As can be seen in Figure 14, the inner surface actuation length of 5 mm has the same trend as the inner surface actuation lengths of 20 mm and 10 mm, and the induced velocity generated by the DBD plasma actuation increases with the increase in the actuation voltage. However, the excellent effect of plasma actuation in Figure 14a is not obvious due to the small actuation dimension. In addition, the kerosene droplets in Figure 14b appear on the inner side of the V-groove fin plate under the action of the induced jet, which is beneficial for the contact between the kerosene and the air and the improvement of the efficiency of kerosene evaporation and combustion. For working condition (c), the induced velocity is too large, resulting in the kerosene droplets failing to reach the V-groove fin plate wall surface under the action of the induced jet. In addition, the kerosene droplets are propelled away from the flameholder by the plasma induced jet, which is not conducive to ignition and combustion.

3.2.3. Actuation Positions

This section examines the effects of different DBD plasma actuation positions on the spray field, and it compares and analyzes the gas-phase flow field and kerosene droplet distribution at different actuation positions.

For the plasma actuation with an inner surface actuation length of 10 mm, two different positions are arranged on the inner surface of the V-groove fin plate (actuation parameters are shown in Table 6), as presented in Figure 15.
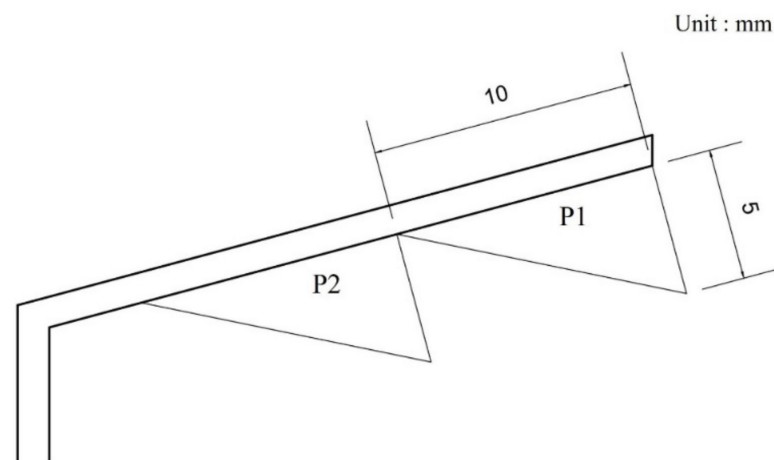
Figure 15. Schematic diagram of different actuation positions with 10 mm actuation length on inner surface (upper part).

Table 6. Parameters of different actuation positions with 10 mm actuation length on inner surface.

Positions	Voltage (kV)	Frequency (kHz)
P1	5	14
P2	5	14

The contours of the kerosene droplet and gaseous flow field at different actuation locations for an inner surface actuation length of 10 mm are provided in Figure 16. It can be seen that the actuation at position P1 in Figure 16a makes the kerosene droplets extensively return to cover the whole flameholder, which is conducive to the sufficient contact between the kerosene droplets and the high temperature gas, which is beneficial for the evaporation and combustion of the droplets. As for the actuation at position P2 in Figure 16b, the useful effect of the actuation is less on the spray field, because the induced recirculation region has less interaction with the kerosene droplets.

(**a**)

(**b**)
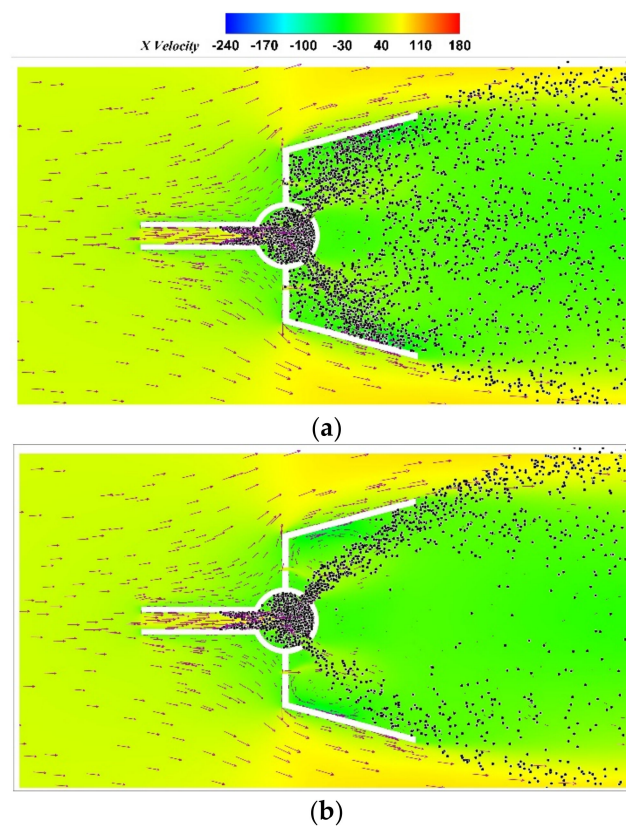
Figure 16. Spray field under different actuation positions with 10 mm actuation length on inner surface: (**a**) P1 position, (**b**) P2 position.

For the plasma actuation with the inner surface actuation length of 5 mm, four different positions are arranged on the inner wall of the V-groove fin plate (actuation parameters are provided in Table 7), as shown in Figure 17.

Table 7. Parameters of different actuation positions with 5 mm actuation length on inner surface.

Positions	Voltage (kV)	Frequency (kHz)
P1	5	14
P2	5	14
P3	5	14
P4	5	14
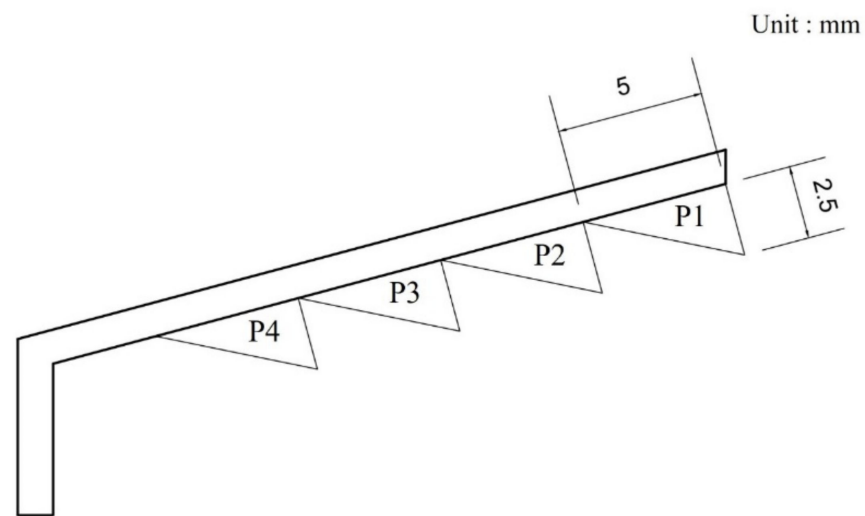
Figure 17. Schematic diagram of different actuation positions with 5 mm actuation length on inner surface (upper part).

The contours of the spray field at different actuation locations for an inner surface actuation length of 5 mm are provided in Figure 18. It is worth noting that the effect of different positions of the DBD plasma actuation (with 5 mm inner surface actuation length) on the gaseous flow field and kerosene droplets is not significant, which is mainly due to the actuation dimensions being too small, resulting in the velocity of the induced jet and the area of influence not being large.
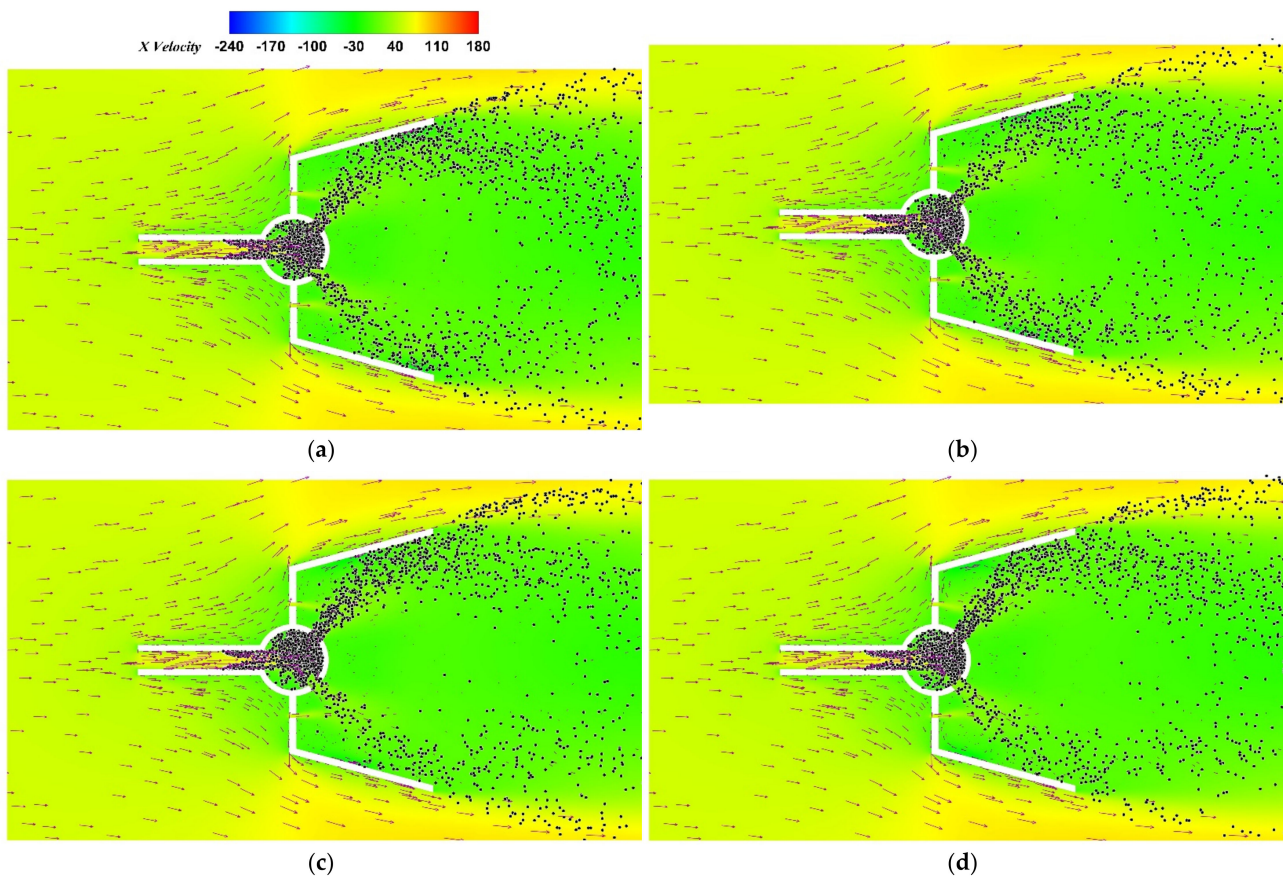
Figure 18. Spray field under different actuation positions with 5 mm actuation length on inner surface: (**a**) P1 position, (**b**) P2 position, (**c**) P3 position, (**d**) P4 position.

In the above study on DBD plasma actuation dimension, intensity, and position effects on the spray field in the subsonic ramjet combustor, it can be found that to obtain a better actuation effect, the velocity of the flow induced by the DBD plasma actuation must be close to the velocity of the flow out of the evaporation tube, and the position of the induced jet must coincide with the position of the kerosene spray reaching the inner surface of the V-groove fin plate. The relative optimal parameters are an inner surface actuation length of 10 mm at position P1, a voltage of 5 kV, and a frequency of 14 kHz. The overall contour of the flow field is shown in Figure 16a and the local flow field is shown in Figure 19.

It is observed in Figure 19a that kerosene droplets are fully distributed in the V-groove near the vertical walls when plasma actuation is applied. The kerosene droplets stay in the V-groove for a long time and are in contact with the high-temperature gas for a long time, which is convenient for the evaporation and combustion of kerosene. In Figure 19b, the wall jet velocity generated by the plasma actuation is about −40 m/s. Since the actuation position is at P1, and the actuation dimension is not too large, the influence of the induced jet on the flow is smaller near the vertical wall of the V-groove, and the same conclusion can be drawn from the fact that the velocity in the y-direction in this region is close to 0 m/s in Figure 19c. In Figure 19d, the recirculation region—under the joint action of the actuation-induced wall jet, the vertical wall inlet jet, and the evaporation tube outlet jet—is once again demonstrated by velocity vector as is shown in Figure 19b,c. The low-temperature region in Figure 19f indicates the denser region of kerosene droplets, and the kerosene droplets with actuation also flow to the upper right after exiting the evaporation tube under the effect of the recirculation region, but the angle is smaller compared to the one with non-actuation, which is beneficial for the better distribution of kerosene droplets. In all, a relatively optimal turbulent mixing of fuel droplets and oxidant air is achieved using the above-mentioned set of DBD plasma actuation parameters.

(**a**)

Figure 19. *Cont.*

(**b**)

(**c**)

(**d**)

Figure 19. *Cont.*

(**e**)
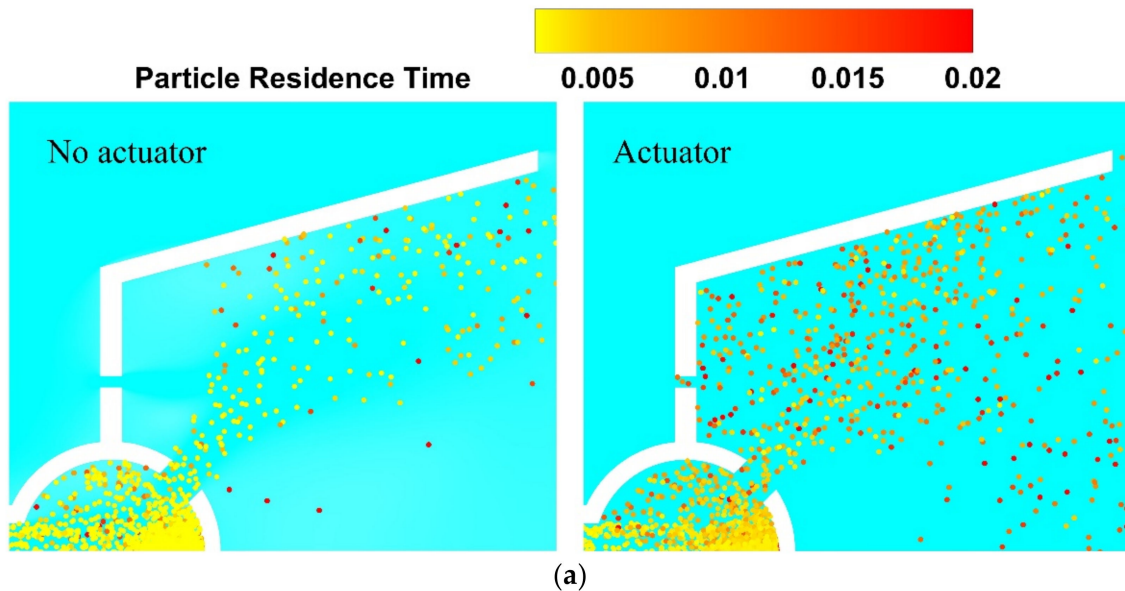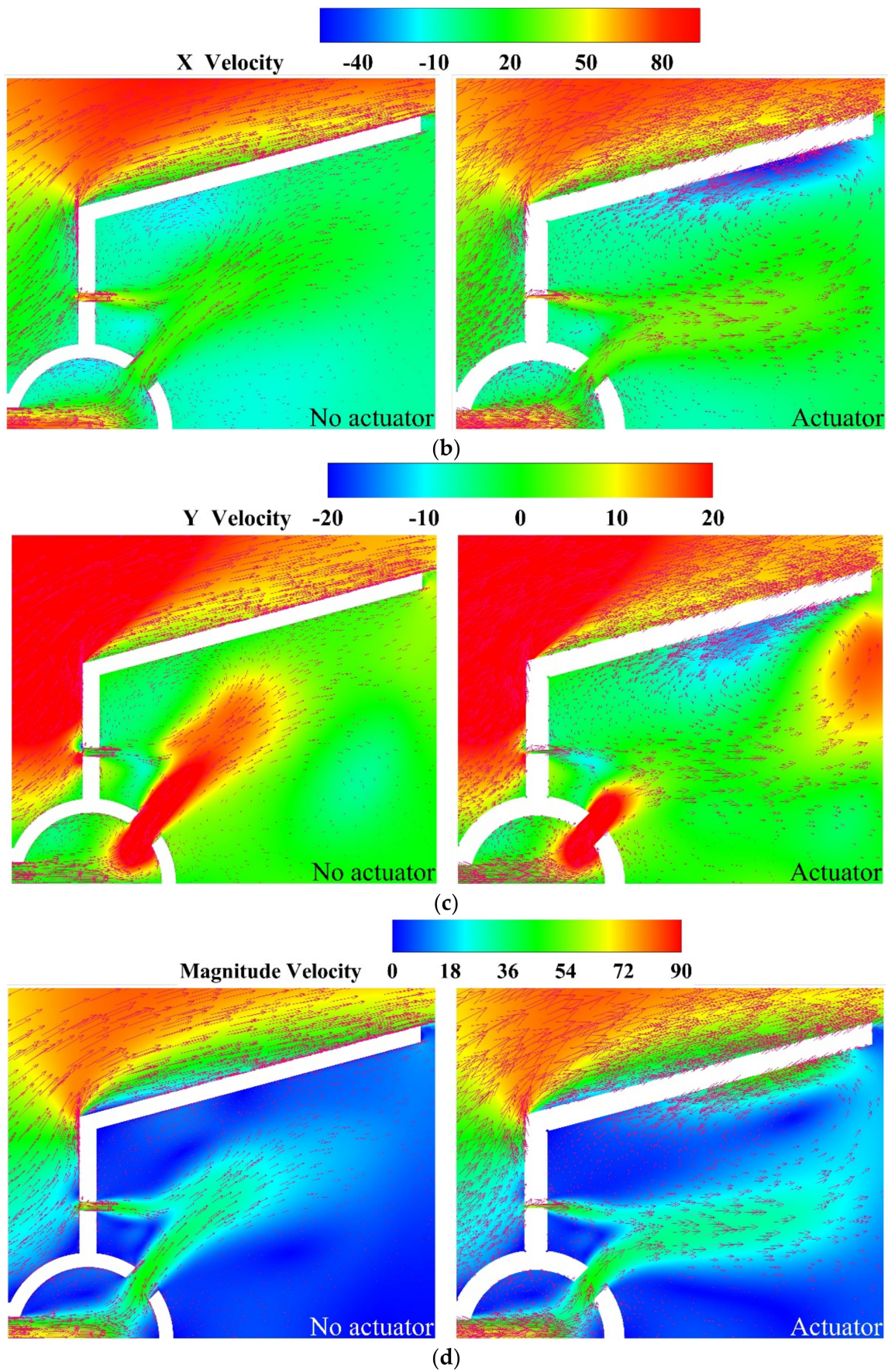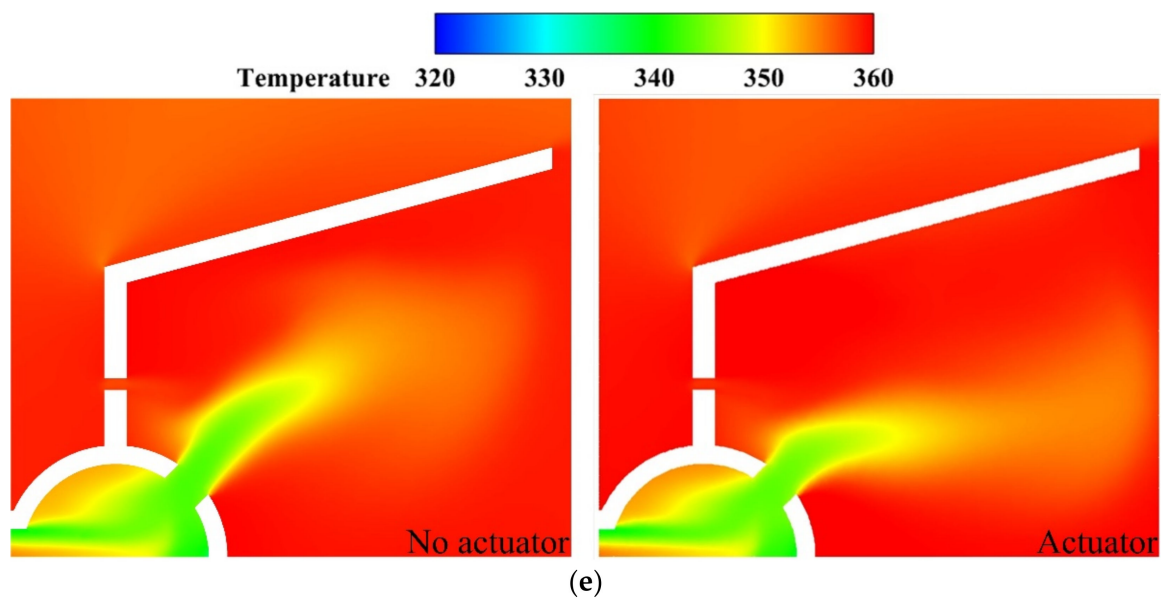
Figure 19. Comparison under non-actuation and actuation. (**a**) Kerosene droplet distribution; (**b**) X direction velocity; (**c**) Y direction velocity; (**d**) magnitude velocity; (**e**) temperature contour.

4. Conclusions

Herein, a DBD plasma actuation study was conducted for the turbulent mixing of fuel droplets and oxidant air in a subsonic combustion ramjet combustor, and the conclusions are as follows:

(1) Comparing the cases with and without plasma actuation, it can be observed that DBD plasma actuation has a significant effect on the spray field because DBD plasma actuation causes a significant change in the velocity near the inner wall surface of the evaporative V-groove flameholder fin plate, which in turn causes an important change in the recirculation regions inside the flameholder and causes a prominent change in the turbulent mixing of fuel droplets and oxidant air.

(2) DBD plasma actuation dimension, intensity, and position all affect the air flow and droplet movement in the evaporative V-groove flameholder. When the actuation dimension decreases, the effect is reduced; when the actuation intensity increases, the effect is an increase; and when the actuation position changes, the air flow and droplet movement vary accordingly.

(3) By adjusting the DBD plasma actuation parameters, relatively optimal turbulent mixing of fuel droplets and oxidant air can be achieved.

Author Contributions: Investigation, formal analysis, and writing—original draft, Z.T.; conceptualization, methodology, formal analysis, writing—review, writing—revision, and supervision, Q.C.; editing—original draft, X.N.; editing—original draft, Z.L.; investigation, H.Y. All authors have read and agreed to the published version of the manuscript.

Institutional Review Board Statement: Not applicable.

Informed Consent Statement: Not applicable.

Data Availability Statement: Not applicable.

Conflicts of Interest: The authors declare no conflict of interest.

References

1. Xu, J.M. Experimental Study and Numerical Simulation of Flameholder in Ramjet Combustors. Master's Thesis, Xidian University, Xi'an, China, 2007.
2. Hong, L.; Yang, G.H. Effects of Incoming Mach Number and Air Excess Coefficient on the Combustion Characteristics of Flameholder. *Adv. Aeronaut. Sci. Eng.* **2010**, *1*, 173–177.
3. Ding, Z.B.; Jin, J. Investigation on Aerodynamic and Combustion Characteristics of an Evaporating Flame-holder. *J. Rocket. Propuls.* **2013**, *39*, 27–31.
4. Ding, Z.B.; Jin, J. Numerical Investigation on Combustion Characteristics and Fuel Supply Matching for an Evaporative Flame-holder. *J. Rocket. Propuls.* **2012**, *38*, 43–48.
5. Jin, L.; Tan, Y.H. Numerical Prediction of Cold Flow Field behind a Vapor Flameholder. *J. Rocket. Propuls.* **2007**, *33*, 23–27.
6. Liu, R.; Liu, Y.Y.; Gao, Z. Structural Parameters Effects on Lean Blowout Performance and Prediction Method for Piloted Vaporization Flameholder. *J. Propuls. Technol.* **2017**, *38*, 2753–2760.
7. Li, Y.; Wu, Y. Research Progress and Outlook of Flow Control and Combustion Control Using Plasma Cctuation. *Sci. Sin. Technol.* **2020**, *50*, 1252–1273. [CrossRef]
8. Zhang, P.; Liu, A.; Wang, J. Flow Structures in Flat Plate Boundary Layer Induced by Pulsed Plasma Actuation. *Sci. China Technol. Sci.* **2010**, *53*, 2772–2782. [CrossRef]
9. Shyy, W.; Jayaraman, B.; Andersson, A. Modeling of Glow Discharge-induced Fluid Dynamics. *J. Appl. Phys.* **2002**, *92*, 6434–6443. [CrossRef]
10. Zhang, D.; Wang, Y.; Wang, D. The Nonlinear Behaviors in Atmospheric Dielectric Barrier Multi Pulse Discharges. *Plasma Sci. Technol.* **2016**, *18*, 826–831. [CrossRef]
11. Yu, J.; Yu, J.; Chen, F.; Wang, C. Numerical Study of Tip Leakage Flow Control in Turbine Cascades Using the DBD Plasma Model Improved by the Parameter Identification Method. *Aerosp. Sci. Technol.* **2019**, *84*, 856–864. [CrossRef]
12. Yu, J.; Liu, H.; Wang, R.; Chen, F. Numerical Study of the flow Structures in Flat Plate and the Wall-Mounted Hump Induced by the Unsteady DBD Plasma. *Plasma Sci. Technol.* **2017**, *19*, 015502. [CrossRef]
13. Shan, H.; Lee, Y.T. Numerical Modeling of Dielectric Barrier Discharge Plasma Actuation. *J. Fluids Eng.* **2016**, *138*, 051104. [CrossRef]
14. Iqbal, M.M.; Turner, M.M. Influence of Gap Spacing between Dielectric Barriers in Atmospheric Pressure Discharges. *Contrib. Plasma Phys.* **2015**, *55*, 444–458. [CrossRef]
15. Wang, C.; Zhang, G.; Wang, X. Comparisons of Discharge Characteristics of a Dielectric Barrier Discharge with Different Electrode Structures. *Vacuum* **2012**, *86*, 960–964. [CrossRef]
16. Sokolova, M.V.; Voevodin, V.V.; Malakhov, J.I.; Aleksandrov, N.L.; Anokhin, E.M.; Soloviev, V.R. Barrier Properties Influence on the Surface Dielectric Barrier Discharge Driven by Single Voltage Pulses of Different Duration. *J. Phys. D Appl. Phys.* **2019**, *52*, 324001. [CrossRef]
17. Moussaoui, A.; Kachi, M.; Zouaghi, A.; Zouzou, N. Neutralization of Charged Dielectric Materials Using a Dielectric Barrier Discharge. *J. Electrost.* **2017**, *87*, 102–109. [CrossRef]
18. Malanichev, V.E.; Malashin, M.V.; Moshkunov, S.I.; Khomich, V.Y. Dielectric Barrier Discharge Plasma Reactor. *High Energy Chem.* **2016**, *50*, 304–307. [CrossRef]
19. Liu, Z.; Yang, L.; Wang, Z.; Sang, L.; Zhu, Q.; Li, S. Atmospheric Pressure Radio Frequency Dielectric Barrier Discharges in Nitrogen/Nrgon. *Plasma Sci. Technol.* **2013**, *15*, 871. [CrossRef]
20. Kim, J.; Kim, S.-J.; Lee, Y.N.; Kim, I.T.; Cho, G. Discharge Characteristics and Plasma Erosion of Various Dielectric Materials in the Dielectric Barrier Discharges. *Appl. Sci.* **2018**, *8*, 1294. [CrossRef]
21. Khomich, V.Y.; Malanichev, V.E.; Malashin, M.V.; Moshkunov, S.I. Dielectric Barrier Discharge Uniformity Enhancement by Air Flow. *IEEE Trans. Plasma Sci.* **2016**, *44*, 1349–1352. [CrossRef]
22. Aerts, R.; Somers, W.; Bogaerts, A.J.C. Carbon Dioxide Splitting in a Dielectric Barrier Discharge Plasma: A Combined Experimental and Computational Study. *ChemSusChem* **2015**, *8*, 702–716. [CrossRef] [PubMed]
23. Zhu, P.; Dong, L.; Yang, J.; Li, B.; Zhang, C. Vibration of Discharge Filaments in a Dielectric Barrier Discharge. *IEEE Trans. Plasma Sci.* **2014**, *42*, 1990–1994. [CrossRef]
24. Zhang, S.; Chen, Z.; Zhang, B.; Chen, Y. Numerical Investigation on the Effects of Dielectric Barrier on a Nanosecond Pulsed Surface Dielectric Barrier Discharge. *Molecules* **2019**, *24*, 3933. [CrossRef] [PubMed]
25. Peeters, F.J.J.; Rumphorst, R.F.; Van de Sanden, M.C.M. Dielectric Barrier Discharges Revisited: The Case for Mobile Surface Charge. *Plasma Sources Sci. Technol.* **2016**, *25*, 03LT03. [CrossRef]
26. Pang, L.; He, K.; Di, D.X. Effect of Pulse Polarity on Nanosecond Surface Dielectric Barrier Discharge. *IEEE Trans. Plasma Sci.* **2014**, *42*, 2340–2341. [CrossRef]
27. Osawa, N.; Yoshioka, Y.; Hanaoka, R.; Mochizuki, Y.; Kobayashi, Y.; Yamada, Y. Generation of Uniform Discharge by Dielectric Barrier Discharge Device in Atmospheric-Pressure Air. *Electr. Eng. Jpn.* **2012**, *180*, 1–9. [CrossRef]
28. Huang, Z.; Yang, L.; Hao, Y.; Li, L. Dynamic Characteristics of Dielectric Barrier Columnar Discharge During Its Decay. *IEEE Trans. Plasma Sci.* **2016**, *44*, 2568–2575. [CrossRef]
29. Bouchikhi, A. Dielectric Barrier Discharge Effect on Capacitively Coupled RF Argon Glow Discharge. *Indian J. Pure Appl. Phys.* **2022**, *60*, 163–170.

30. Ombrello, T.; Won, S.H.; Ju, Y.; Williams, S. Flame propagation enhancement by plasma excitation of oxygen. Part II: Effects of O2 (a1Δg). *Combust. Flame* **2010**, *157*, 1916–1928. [CrossRef]
31. Jin, D.; He, L.; Liu, X.; Chen, Y. Numerical simulation of plasma-assisted combustion of methane-air mixtures in combustion chamber. *Plasma Sci. Technol.* **2018**, *20*, 125502.
32. Cui, W.; Ren, Y.; Li, S. Stabilization of premixed swirl flames under flow pulsations using microsecond pulsed plasmas. *J. Propuls. Power* **2019**, *35*, 190–200. [CrossRef]
33. Huang, S.; Wu, Y.; Zhang, K.; Sun, J.; Jin, D.; Li, Y. Experimental Investigation on Spray and Ignition Characteristics of Plasma Actuated Bluff Body Flameholder. *Fuel* **2022**, *309*, 122215. [CrossRef]
34. Abdollahzadeh, M.; Páscoa, J.; Oliveira, P. Numerical modeling of boundary layer control using dielectric barrier discharge. In Proceedings of the IV Conferência Nacional em Mecânica dos Fluidos, Termodinâmica e Energia, MEFTE, Lisbon, Portugal, 28–29 May 2012.